Effects of Electrolyte Buffer Capacity on Surface Reactant Species and Reaction Rate of CO_2 in Electrochemical CO_2 Reduction

Hiroshi Hashiba,[1] *Lien-Chun Weng,*[2,3] *Yikai Chen,*[4] *Hiroki K. Sato,*[1] *Satoshi Yotsuhashi,*[1] *Chengxiang Xiang,*[4] *Adam Z. Weber*[*2]

[1] Advanced Research Division, Panasonic Corporation, Sōraku-gun, Kyoto 619-0237, Japan

[2] Joint Center for Artificial Photosynthesis, Lawrence Berkeley National Laboratory, Berkeley, CA 94720, USA

[3] Department of Chemical and Biomolecular Engineering, University of California, Berkeley, CA 94720, USA

[4] Joint Center for Artificial Photosynthesis, California Institute of Technology, Pasadena, CA, 91125, USA

E-mail address: azweber@lbl.gov

<Abstract>

In the aqueous electrochemical reduction of CO_2, the choice of electrolyte is responsible for the catalytic activity and selectivity, although there remains a need for more in-depth understanding of electrolyte effects and mechanisms. In this study, using both experimental and simulation approaches, we report how the buffer capacity of the electrolytes affects the kinetics and equilibrium of surface reactant species and resulting reaction rate of CO_2 with varying partial CO_2 pressure. Electrolytes investigated include KCl (non-buffered), $KHCO_3$ (buffered by bicarbonate), and phosphate buffered electrolytes. Assuming 100% methane production, the simulation successfully explains the experimental trends of maximum CO_2 flux in KCl and $KHCO_3$, and also highlights the difference between $KHCO_3$ and phosphate in terms of pKa as well as the impact of buffer capacity. To examine the electrolyte impact on selectivity, the model is run with a constant total current density. Using this model, several factors are elucidated including the importance of local pH, which is not in acid/base equilibrium, the impact of buffer identity and kinetics, and the mass-transport boundary-layer thickness. The gained understanding can help optimize CO_2 reduction in aqueous environments.

<Introduction>

Electrochemical CO_2 reduction (CO_2R) is one of the key technologies to realize a sustainable society by converting emitted CO_2 to useful chemicals and fuels if combined with surplus energy sources like solar or wind power. For decades, a number of researchers have shown that some transition metals can catalyze CO_2 to more reduced products like carbon monoxide (CO), formic acid or formate (HCOOH or $HCOO^-$, respectively), hydrocarbons, alcohols, and other organic materials[1-4] that can be used for renewable chemicals and fuels.[5-6]

Although a variety of useful chemicals can be produced from CO_2, selectivity control for the desired product is still difficult in CO_2R, especially highly reduced products such as hydrocarbons and alcohols.[3] Moreover, the necessary high surface overpotential and possible competing reactions such as hydrogen-evolution reaction (HER) are problems that prevent practical application of this technology.[7] One route towards overcoming these problems is to make an efficient catalyst that lowers the overpotential with high selectivity for CO_2R.[8-11] Another way is to manipulate the system parameters to realize the optimum condition for CO_2R catalyst, which has been shown to affect significantly the rate and selectivity of CO_2R reaction.[7, 12-17]

Among the parameters that affect the property of CO_2R, the electrolyte composition is known to be an important factor. In this research field, potassium bicarbonate ($KHCO_3$) and potassium chloride (KCl) solutions are the most commonly used aqueous electrolytes.[1, 18-20] While it is evident that the selectivity of CO_2R is extremely sensitive to the local conditions and concentrations, properties of the ionic electrolytes in controlling these conditions are often

overlooked.[21-23] In comparing $KHCO_3$ and KCl, one of the most important differences is their buffering capacity, where $KHCO_3$ is a buffered electrolyte while KCl is not. The buffered electrolyte could compensate for the hydroxide ions (OH^-) produced by CO_2R and HER, and maintain the electrode surface pH close to the bulk value during the electrolysis.[24] Minimizing the pH difference between surface and the bulk can minimize polarization losses, [15] as well as affect the product distribution.[7] The authors have recently found that the methane (CH_4) production rate from CO_2R is significantly increased by simply using 0.5 M $KHCO_3$ instead of 0.5 M KCl with a polycrystalline copper (Cu) catalyst.[17] This strongly indicates that the choice of a buffered electrolyte like 0.5 M $KHCO_3$ is one of the important factors to increase the reaction rate of CO_2R, although the origins of such an enhancement remain unknown. To obtain a comprehensive understanding of how the choice of electrolyte affects the activity and selectivity of CO_2R, a detailed analysis of the electrolyte speciation and concentrations, including the pH, CO_2 concentration, *etc*, near the electrode surface is required.

In this study, the effects of buffered electrolytes were investigated using both experimental and simulation approaches. The limiting reaction rates of CO_2, J_{lim}, defined by the authors in a previous report,[16] at various partial CO_2 pressures (P_{CO2}) and electrolyte compositions were obtained both experimentally and from a one-dimensional (1-D) model. The model enables one to examine concentrations and effects at and near the electrode surface and is used to explain the experimental trends of J_{lim} vs P_{CO2}.

<Experimental>

For all of the experiments in this study, a “combinatorial system” is used to perform eight experiments in parallel with changing parameters such as stirring speed, reaction voltage (or current density), P_{CO2}, and temperature. More details about this system are described in our previous report.[16] We used strip-shaped Cu plates (Nilaco, Japan, 99.99%) with an active surface area of 1 cm^2 as the cathode electrode for CO_2R. The surface was chemically polished using a mixture of nitric acid and phosphoric acid (S-710, Sasaki Chemical, Japan). Platinum wire (BAS, Japan) was used as the anode electrode and saturated Ag/AgCl (Corr instruments, US) was used as the reference electrode. Each cell was divided into cathode and anode compartments with Nafion 424 (Aldrich, US). The cathode electrolytes were 0.5 M KCl (Wako, Japan) or 0.5 M $KHCO_3$ or a 1 M phosphate buffer solution (0.7 M K_2HPO_4: 0.3 M KH_2PO_4), whereas the anode electrolyte was the same at 3.0 M $KHCO_3$ (Wako, Japan). The phosphate buffer species were chosen to yield a bulk pH of around 7 in the absence of CO_2.[25]

Prior to an experiment, each reactor was first bubbled with Ar and then with CO_2, each for 60 min and with a flow rate of 125 sccm (standard cubic centi meter per minute). The reactors were then pressurized with CO_2 to the experimental values. Electrochemical measurements were performed to ascertain the current density while also controlling the stirring speed inside the reactor. Galvanostatic measurements with BT2000 (Arbin, US) multi-channel potentiostats were performed up to 100 C, with a different current density set in each reactor used to obtain the current density dependence of the product distribution for each single experimental condition. All experiments were done at 25°C. After the measurements, gas samples were transferred to a 7890A (Agilent, CA, USA) gas chromatograph (GC), which quantitatively analyzed the reaction products (TCD for hydrogen (H_2), and FID for CO (with methanizer), CH_4, and ethylene (C_2H_4)) For the analysis of liquid samples, we used a Prominence

(Shimadzu, Japan) high-performance liquid chromatography (HPLC) for $HCOO^{-}$ detection and a GC-17A (Shimadzu, Japan) with a TurboMatrix40 (PerkinElmer, MA, USA) headspace system (HS-GC) for the detection of aldehydes and alcohols. The Faradaic efficiency (FE) is determined by dividing the charge ascribed to each product by the total charge passed. The reaction rate of CO_2, J_{CO2}, is given by

$$J_{CO2} = \sum_p J_p = \frac{1}{F} \sum_p \frac{n \times i_{PCD}}{z} \quad (1)$$

where z and n represent the numbers of electrons and reactants necessary for the reaction, respectively, and F represent Faraday's constant. The subscript p denotes a reaction product from CO_2, and i_{PCD} is the partial current density of each product (the product of the total current density and FE). J_{lim} is determined as the maximum value of J_{CO2} as plotted against current density.

<Simulation>

A one-dimensional, isothermal, steady-state model simulates the hydrodynamic boundary layer region near the electrode (see Figure 1). The boundary layer thickness was set to be 100 μm for the base case, and varied to examine boundary-layer thickness effects. There is no convection within the hydrodynamic boundary layer, and the double-layer region, where electroneutrality does not hold, is neglected as it is very thin in these electrolytes. The species in the system are:

dissolved CO_2, K^+, H^+, OH^-, HCO_3^-, CO_3^{2-}. Additionally, there is Cl^- for KCl electrolyte, and $H_2PO_4^-$, HPO_4^{2-}, and PO_4^{3-} for the potassium-phosphate buffer electrolyte.

The flux of each species, N_i, is calculated using the Nernst-Planck equation, accounting for migration and diffusion,

$$N_i = -D_i \nabla c_i - z_i \frac{D_i}{RT} F c_i \nabla \phi_l \tag{2}$$

where D_i and c_i, and z_i are the diffusivity, concentration, and charge of species i, respectively, and ϕ_l is the liquid potential.

Component balances at steady state yield

$$\nabla \cdot N_i = R_i \tag{3}$$

where R_i is the source term for species i. Within the electrolyte, the bicarbonate acid/base, phosphate acid/base (for phosphate buffer cases) and water-dissociation reactions contribute to the source term according to

$$CO_2 + H_2O \underset{k_{-1}}{\overset{k_1}{\leftrightarrow}} H^+ + HCO_3^- \quad -, K_1 = 10^{-6.35}$$

$$HCO_3^- \underset{k_{-2}}{\overset{k_2}{\leftrightarrow}} H^+ + CO_3^{2-} \quad 2-, K_2 = 10^{-10.33}\, M$$

$$CO_2 + OH^- \underset{k_{-3}}{\overset{k_3}{\leftrightarrow}} HCO_3^- \quad -, K_3 = K_1 / K_w$$

$$2-¿,K_4=K_2/K_W$$
$$-¿\,k_4,k_{-4}\,H_2O+CO_3^{¿}$$
$$\leftrightarrow$$
$$-¿+OH^{¿}$$
$$HCO_3^{¿}$$

$$2-¿,K_5=10^{-7.21}M^{-1}$$
$$+¿+HPO_4^{¿}$$
$$-¿\,k_5,k_{-5}\,H^{¿}$$
$$\leftrightarrow$$
$$H_2PO_4^{¿}$$

$$3-¿,K_6=10^{-12.32}M^{-1}$$
$$+¿+PO_4^{¿}$$
$$2-¿\,k_6,k_{-6}\,H^{¿}$$
$$\leftrightarrow$$
$$HPO_4^{¿}$$

$$+¿+OH^{-¿,K_w=10^{-14}M^2}$$
$$¿$$
$$H_2O\,k_w,k_{-w}\,H^{¿}$$
$$\leftrightarrow$$

where k_j and k_{-j} are the forward (left to right) and reverse (right to left) rate constants and K_j is the equilibrium coefficient for reaction j. The forward rate constants for the bicarbonate acid/base and water dissociation reactions are listed in Table S1.[26] We assumed equilibrium for the phosphate buffer reactions and take the rate constants, k_5, k_6 to be large (10^6 s^{-1}). The backwards rate constants are then calculated from the relationship

$$k_{-i}=\frac{k_i}{K_i} \tag{4}$$

Two conditions were investigated: (1) 100% CH_4 conversion, and (2) 90 mA/cm^2 total current density. The boundary conditions are listed in Table 1, where i_T is the total current density (set to 90 mA/cm^2 based on experimental data, Figure S3), k_{m_i} is the mass-transfer coefficient of species i at the bulk electrolyte/boundary layer boundary. k_{m_i} is taken to be a

large value, and estimated using $\frac{D_i}{1\,\mu m}$, to allow fast equilibration for each species with its bulk concentration.

The set of differential and algebraic equations are solved simultaneously using the MUMPS solver in COMSOL 5.2a. Instability occurs at high current densities so we solve low current density conditions first and use them as the initial guesses for high current-density conditions.

<Results and Discussions>

While it is known that the use of $KHCO_3$ results in higher FE as a function of current density compared to KCl (see Figure S1), the mechanism and causality are not definitively determined. There are two possible explanations for this phenomenon: (1) The anion in the electrolyte (Cl^- vs HCO_3^-) is affecting the kinetics of the reaction, possibly by interacting with reaction intermediates on the catalyst surface,[27] (2) The buffering capacity of $KHCO_3$ is affecting species concentration near the electrode surface, in particular changing the pH and the concentration of CO_2 at the electrode surface. To investigate the mass-transport effects of this system, the pressure dependence of the limiting CO_2 flux (the rate of CO_2 consumption where the CO_2 mass-transport is rate-determining-step (CO_2 limited conditions)) for the two electrolytes is compared. At CO_2 limited conditions, the rate of CO_2 consumption should be independent of catalyst kinetics, allowing a direct comparison of mass-transport limitations of systems with different electrolytes.

Since Cu reduces CO_2 to multiple products requiring different number of electrons, we cannot directly compare the limiting current density (LCD) between cases. Instead of LCD, we use our previously-defined "limiting rate of mass transport" (J_{lim}) to characterize the maximum rate of CO_2 consumption.[16] J_{lim} describes the rate of CO_2 flux to the electrode surface at limiting conditions (i.e. local CO_2 concentration becomes zero). At CO_2 limited conditions, the rate of CO_2 flux to the electrode surface should be equal to the rate of CO_2R. Figure 2 shows the pressure dependent J_{lim} in 0.5 M $KHCO_3$ and 0.5 M KCl electrolyte. As seen from the figure, J_{lim} in $KHCO_3$ is higher than in KCl at the same P_{CO2}. Moreover, the data points for J_{lim} in $KHCO_3$ increases nonlinearly with P_{CO2}, whereas in KCl, J_{lim} increases almost linearly from the zero point, consistent with our previous report.[16] This indicates that the behavior of J_{lim} in $KHCO_3$ could not be simply explained by the dissolved amount of CO_2 increasing with pressure, in which case J_{lim} should increase proportionally with CO_2 concentration in the electrolyte according to Fick's and Henry's laws.

To investigate further the origin of such characteristic behavior of J_{lim} in $KHCO_3$ and KCl electrolyte, a 1-D simulation model was employed assuming 100% CH_4 production from CO_2. As shown in Figure 1, the model simulates mass transport of each species within the boundary layer between the catalyst surface (point A, local) and bulk electrolyte (point B, bulk). As stated above, different conditions were modeled including the experimentally used conditions: 0.5 M KCl and 0.5 M $KHCO_3$, as well as two additional cases: 1 M phosphate buffer (mixture of 0.3 M KH_2PO_4 and 0.7 M K_2HPO_4) and 1.5 M $KHCO_3$, to demonstrate how using an electrolyte with a stronger buffer capacity might improve CO_2 transport to the catalyst surface. It should be noted that a direct comparison of the two buffers is complicated by the fact that CO_2 will always result in some bicarbonate buffering as shown in Figure S2. Figure 3a shows the simulation result of P_{CO2}

dependence of J_{lim}. Comparing the different electrolytes, one can see that for both the bicarbonate and phosphate buffers, J_{lim} initially follows Fick's law at low CO_2 reaction rates (low P_{CO2}), with the phosphate buffer and 1.5 M $KHCO_3$ system deviating from Fick's law at a slightly higher P_{CO2} compared to 0.5 M $KHCO_3$ and 0.5 M KCl. In contrast, J_{lim} for KCl increases proportionally with P_{CO2} with a slope much smaller than that expected by Fick's law (i.e., diffusion without reactions). Comparing Figure 2 and Figure 3a, the simulation qualitatively reproduces the nonlinear behavior of J_{lim} seen in experiments with 0.5 M $KHCO_3$. As shown in Figure 3b and 3c, this behavior is derived from the changes in pH and local CO_2 concentration. The CO_2 concentration profile deviates from Fick's law in both electrolytes, with a smaller slope (i.e. smaller CO_2 flux) near the electrode surface compared to what is predicted from Fick's law. This slope determines the rate of CO_2 supplied to the electrode, J_{lim}. The deviation from Fick's law is caused by the consumption of CO_2 by OH^- produced during the electron transfer reactions (for each electron consumed one OH^- is produced). As shown in Figure 3c, the bulk pH in 0.5 M KCl and 0.5 M $KHCO_3$ at CO_2-saturated condition is ~3.6 and ~7.0, respectively, which agree with experimental observations.[16, 28] However, as the electrode surface is approached, the pH in both electrolytes rises significantly. Considering acid/base reactions, CO_2 is less likely to be present at alkaline conditions (see reactions above),[15] where OH^- produced through CO_2R reacts with CO_2 to produce HCO_3^- and CO_3^{2-}, which are generally considered not to be reactants for CO_2R.[24] In a buffered system (e.g. $KHCO_3$), the pH within the boundary layer can be somewhat maintained to remain close to bulk pH. In contrast, for the unbuffered KCl system, the pH near the electrode is drastically increased (Figure 3c). These pH effects and impact of buffering capacity can be used to explain the other curves in Figure 3a. Using a stronger buffer, either higher concentration

bicarbonate buffer or phosphate buffer, J_{lim} further increases and approaches Fick's law, due to the lower pH attained at the surface of the electrode (see Figure 3c).

To explore these effects in more detail, J_{lim} is normalized by the value estimated under Fick's law and plotted as a function of the pH difference from bulk electrolyte to electrode surface under the CO_2 mass-transport-limited conditions in Figure 4. This figure clearly illustrates the general linkage between buffering property of the electrolyte and the limiting rate of CO_2R. Figure 4 predicts that buffer strength of the electrolyte is one of the design guidelines to achieve high reaction rate in CO_2R, where the mass-transport of CO_2 is one of the rate-determining factors.[14, 16] Interestingly, while both 1 M phosphate buffer and 1.5 M $KHCO_3$ give a limiting flux greater than 60% maximum flux (Fick's law prediction), and maintains the surface pH to be within 4 units of the bulk pH, they do not follow the same trend. The reason for this is the difference in pKa values for the two buffers. Comparing the pH profiles for 1.5 M $KHCO_3$ and 1 M phosphate buffer (Figure 3c), we can see that bicarbonate buffer maintains the pH near 10, while phosphate buffer electrolyte has two distinct regions of stable pH: one near pH 7.5 and the other near pH 11. These results indicate that both the buffering capacity, and the pKa values of the buffer chosen can affect the pH, and therefore CO_2 supply to the electrode.

From the simulation results shown above, phosphate buffer could be better than KCl and $KHCO_3$ in terms of CO_2 mass-transfer due to its stronger buffer capacity and its ability to react with the produced hydroxide without impacting the CO_2 from the bicarbonate equilibrium directly (i.e., it in essence helps to decouple these phenomena). To see the effect of phosphate buffer experimentally, a series of experiments with varying P_{CO2} in 1 M phosphate buffer solution (0.7 M K_2HPO_4: 0.3 M KH_2PO_4) were conducted. Interestingly, the plot of J_{lim} in phosphate buffer solution shows a downward-convex shape and the value of J_{lim} in each P_{CO2} is less than

that in 0.5 M $KHCO_3$ as shown in Figure 5. This behavior is different than that predicted, indicating other factors may be occurring including perhaps not 100% conversion to methane and also possibly the existence of unaccounted phenomena such as differences in catalyst selectivity due to phosphate interactions, which has been witnessed on copper previously.[21]

While 100% CH_4 is the most ideal case, it is known that the current catalysts produce various reduction species including H_2, CO, C_2H_4, etc. Except for $HCOO^-$, all of the other electron transfer products produce one OH^- per e^- consumed, which impacts the local pH at the electrode surface. For example, Figure S5 shows how the limiting CO_2 flux increases with CH_4 FE assuming that the catalyst produces only CH_4 and H_2 for the 1 M phosphate buffer case at 1 atm CO_2 assuming that the local CO_2 concentration at the electrode is 0. The total current density decreases as CH_4 FE increases since it switches from a two-electron process for HER to an eight-electron process for CH_4 production. The lower total current density produces less OH^-, which explains the increase in limiting CO_2 flux, and highlights the importance of overall hydroxide generation rate.

To account for the selectivity and better match experimental conditions, we considered a model where the total current density was fixed without specifying the product distribution (i.e., the OH^- flux is linearly proportional to the total current density). For the total current density, 90 mA/cm^2 was chosen as it represented the total current density at which maximum CO_2 flux was achieved during experiments (see Figure S3). Figure 6(a) shows the comparison of the simulation results between the 100% CO_2R to CH_4 and constant OH^- flux models for a boundary layer thickness of 100 μm. As previously discussed, J_{lim} shows a concave dependence on P_{CO2} for the 100% CO_2R model, but a downward-convex behavior with pressure for the constant OH^-

flux model. The difference is due to the way in which the pH changes with current density in that the current (and thus OH^- production) is increasing with the 100% CH_4 model, whereas it is fixed in the 90 mA/cm^2 one. These results highlight the importance of how the model can be used to perhaps diagnose what is occurring near the surface in terms of pH and FE. The crossover point between the models is associated with the case of 90 mA/cm^2 being the limiting current density for 100% CO_2R to CH_4. Moreover, as shown in Figure 6(b), the pressure dependence of J_{lim} is significantly affected by the boundary-layer thickness, where J_{lim} exhibits a linear shape at the thickness of 50 μm but becomes nonlinear at 100 and 150 μm. This result shows that the thickness of boundary layer is also responsible for the qualitative behavior of pressure dependence of J_{lim} with constant OH^- flux model.

To explore the impact of buffer capacity in more detail using this model, different buffers and buffer concentrations associated with bulk pH (see Figure S2) are made in a similar fashion to the simulations above. This provides a good comparison since the total hydroxide generation flux is constant at the total current density and thus the differences in J_{lim} can also be correlated to different FEs. As Figure 7(a) shows, the normalized J_{lim} by Fick's law (similar to Figure 4) as a function of P_{CO2} for various buffer concentrations and identities demonstrates different shapes. Obviously, the increase in buffer concentration plays an important role in controlling the local CO_2 concentration and decreasing the impact of hydroxide, thereby enabling a much more Fickian response. In terms of concentrations, low amounts of bicarbonate result in less buffer capacity, which results in lower performance. As shown in the Figure, this effect is sensitive to CO_2 concentration since increased CO_2 results in increased HCO_3^- and thus buffering capacity. Such a trend is not as strong with phosphate since due to the additional interactions and pKa differences. Figure 7(a) also demonstrates how the identity of the phosphate buffer impacts J_{lim}.

From Figure S2, changing the ratio of K_2HPO_4 and KH_2PO_4 with the same amount of phosphate results in different bulk pH values due to the buffer, which is also impacted by the effective bicarbonate concentration and its buffering by dissolved CO_2 (see Figure S2). Thus, the shaded region in Figure 7(a) indicates how the initial composition and bulk pH of phosphate buffer impact J_{lim}, which have a larger impact at higher concentrations of K_2HPO_4 (i.e. higher effective bicarbonate concentration under CO_2 atmosphere) and eventually resulting in a constant offset as the increased P_{CO2} results in more bicarbonate buffering. Finally, there is a question about how the kinetics of the buffer reactions (see Table S1 and equations above) impact the value of J_{lim}. As shown in Figure 7(b), as the kinetics are decreased for the phosphate buffer reaction, J_{lim} decreases since it is harder for the buffer to mitigate the impact of the constant hydroxide rate, which decreases the CO_2 concentration near to the electrode. At very low rates, the phosphate essentially no longer buffers and a response similar to no buffer (e.g., KCl) or low bicarbonate concentration, which could as well explain some of the differences between experiment and the model. It is important to note that even at the higher rates that are taken from general literature, equilibrium between CO_2 and bicarbonate is not achieved next to the electrode surface (see Figure S4), and in fact varies significantly. These findings highlight that the assumption of equilibrium for the acid/base reactions is incorrect and that there is a need to measure the buffer kinetics in solutions of interest.

As noted above, the boundary-layer thickness is an important factor to determine the behavior of CO_2 mass transport and local CO_2 concentration at the electrode surface. It is expected that one can alter the boundary-layer thickness due to convection as well as just due to hydrogen or other gaseous-product formation. To explore this aspect further in terms of analyzing the experimental data, one can calculate the effective boundary-layer thickness for

limiting current or the effective CO_2 surface concentration using the model and a total current density. Table S2 shows such results from the experimental data of J_{lim} and the measured H_2 FE in 0.5 M KCl and $KHCO_3$ solutions. From the calculations, it is clear that the boundary-layer thickness is on the order of 100 μm or so, but it does vary and so the assumption of 100 μm boundary layer may not be fully correct. This variation is either due to the simplified model or perhaps the effect of the bubbles of H_2 or other gaseous products which is considered to affect the boundary-layer thickness.[29] In addition, in agreement with Figure 2, the current density is much higher for $KHCO_3$ than KCl due to its buffering capacity, although it is interesting to note that the boundary layer is relatively the same between the cases with it being somewhat thinner for $KHCO_3$ due to the higher current densities and thus higher HER rates. The similarity in boundary-layer thicknesses demonstrate as well that the model is capturing the salient physics.

<**Conclusion**>

In this paper, we have demonstrated how the electrolyte buffer capacity and identity in terms of pKa affects CO_2 transport within the boundary layer and the local CO_2 concentration available at the electrode surface for CO_2R. The simple transport model agreed with experimental trends of maximum flux seen for CO_2R on Cu in different electrolytes, although a deviation from the experiment thought to be kinetic in origin existed when a phosphate buffer was used. Comparing the limiting CO_2 flux at different P_{CO2} in KCl and $KHCO_3$, we observe that both systems deviate from Fick's law and $KHCO_3$ gives a higher CO_2 flux than KCl electrolyte due to the improved CO_2 flux in $KHCO_3$ caused by the buffering capacity of bicarbonate, leading to a slower increase in local pH and slower homogeneous consumption of CO_2 by OH^-. This is

especially important at high current densities where OH^- ions are produced in large quantities. The model results showed that the pKa value significantly affects the shape of the pH profile within the boundary layer, which can also be impacted by overall buffer concentrations and kinetics, where equilibrium is not achieved next to the electrode surface. Finally, we considered the case where we increased the P_{CO2} at a constant total current density, and showed that increasing bicarbonate concentration at low pressures (< ~ 2.5 atm) is more effective in improving CO_2 transport when the target product (i.e. CH_4) faradaic efficiency remains high; at high pressures (> ~ 2.5 atm) however, CO_2 transport is improved more rapidly with increased P_{CO2} when the total current density is held constant. This analysis and approach provides insights for how buffer electrolytes affect the mass-transport of CO_2 within the system.

<Supporting Information >

Additional information in the supporting information includes tables for rate constants and additional boundary-layer simulation results, supplemental experimental results, pH calculation of phosphate buffer, the calculation of equilibrium within boundary layer, and the impact of methane faradaic efficiency on total current density using the limiting-current model. The raw data for all figures is also given or referenced. This material is available free of charge via the Internet at http://pubs.acs.org.

<**Acknowledgement**>

The material is based upon work performed by the Joint Center for Artificial Photosynthesis, a DOE Energy Innovation Hub, as follows: The constant flux simulations were supported through the Office of Science of the U.S. Department of Energy under Award No. DE-SC0004993; The experimental work and the limiting-current simulations and analysis were supported by Panasonic Corporation under a JCAP Industrial Partnership Agreement.

<**References**>

1. Hori, Y.; Kikuchi, K.; Suzuki, S., Production of CO and CH_4 in electrochemical reduction of CO_2 at metal electrodes in aqueous hydrogencarbonate solution. *Chem. Lett.* **1985**, 1695-1698.
2. Azuma, M.; Hashimoto, K.; Hiramoto, M.; Watanabe, M.; Sakata, T., Electrochemical reduction of carbon dioxide on various metal electrodes in low-temperature aqueous $KHCO_3$ media. *J. Electrochem. Soc.* **1990,** *137*, 1772-1778.
3. Kuhl, K. P.; Cave, E. R.; Abram, D. N.; Jaramillo, T. F., New insights into the electrochemical reduction of carbon dioxide on metallic copper surfaces. *Energy Environ. Sci.* **2012,** *5*, 7050-7059.
4. Song, Y.; Peng, R.; Hensley, D. K.; Bonnesen, P. V.; Liang, L.; Wu, Z.; Meyer, H. M.; Chi, M.; Ma, C.; Sumpter, B. G.; Rondinone, A. J., High-selectivity electrochemical conversion of CO_2 to ethanol using a copper nanoparticle/N-doped graphene electrode. *ChemistrySelect* **2016,** 1, 6055-6061.
5. Whipple, D. T.; Kenis, P. J. A., Prospects of CO_2 utilization via direct heterogeneous electrochemical reduction. *J. Phys. Chem. Lett.* **2010,** *1*, 3451-3458.
6. Durst, J.; Rudnev, A.; Dutta, A.; Fu, Y.; Herranz, J.; Kaliginedi, V.; Kuzume, A.; Permyakova, A. A.; Paratcha, Y.; Broekmann, P.; Schmidt, T. J., Electrochemical CO_2 reduction – A critical view on fundamentals, materials and applications. *CHIMIA Int. J. Chem.* **2015,** *69*, 769-776.

7. Hori, Y. Electrochemical CO_2 reduction of metal electrodes. In Modern Aspects of Electrochemistry; Vayenas, C. G., White, R. E., Gamboa-Aldeco, M. E., Eds.; Springer: New York, **2008**; pp 89−189.

8. Li, C. W.; Kanan, M. W., CO_2 reduction at low overpotential on Cu electrodes resulting from the reduction of thick Cu_2O films. *J. Am. Chem. Soc.* **2012,** *134*, 7231-7234.

9. Li, C. W.; Ciston, J.; Kanan, M. W., Electroreduction of carbon monoxide to liquid fuel on oxide-derived nanocrystalline copper. *Nature* **2014,** *508*, 504-507.
10. Lu, Q.; Rosen, J.; Zhou, Y.; Hutchings, G. S.; Kimmel, Y. C.; Chen, J. G.; Jiao, F., A selective and efficient electrocatalyst for carbon dioxide reduction. *Nat. Commun.* **2014,** *5*, 3242.
11. Kwon, Y.; Lum, Y.; Clark, E. L.; Ager, J. W.; Bell, A. T., CO_2 electroreduction with enhanced ethylene and ethanol selectivity by nanostructuring polycrystalline copper. *ChemElectroChem* **2016,** 3, 1012-1019.
12. Hori, Y.; Kikuchi, K.; Murata, A.; Suzuki, S., Production of methane and ethylene in electrochemical reduction of carbon dioxide at copper electrode in aqueous hydrogencarbonate solution. *Chem. Lett.* **1986**, 897-898.
13. Hori, Y.; Murata, A.; Takahashi, R., Formation of hydrocarbons in the electrochemical reduction of carbon dioxide at a copper electrode in aqueous solution. *J . Chem. Soc. Faraday Trans. 1* **1989,** *85*, 2309-2326.

14. Hara, K.; Tsuneto, A.; Kudo, A.; Sakata, T., Electrochemical reduction of CO_2 on a Cu electrode under high pressure. *J. Electrochem. Soc.* **1994,** *141*, 2097-2103.
15. Singh, M. R.; Clark, E. L.; Bell, A. T., Effects of electrolyte, catalyst, and membrane composition and operating conditions on the performance of solar-driven electrochemical reduction of carbon dioxide. *Phys. Chem. Chem. Phys.* **2015,** *17*, 18924-36.
16. Hashiba, H.; Yotsuhashi, S.; Deguchi, M.; Yamada, Y., Systematic analysis of electrochemical CO_2 reduction with various reaction parameters using combinatorial reactors. *ACS Comb. Sci.* **2016,** *18*, 203-208.
17. Hashiba, H.; Sato, H. K.; Yotsuhashi, S.; Fujii, K.; Sugiyama, M.; Nakano, Y., A broad parameter range for selective methane production with bicarbonate solution in electrochemical CO_2 reduction. *Sustainable Energy Fuels* **2017,** *1*, 1734-1739.
18. Kuhl, K. P.; Hatsukade, T.; Cave, E. R.; Abram, D. N.; Kibsgaard, J.; Jaramillo, T. F., Electrocatalytic conversion of carbon dioxide to methane and methanol on transition metal surfaces. *J. Am. Chem. Soc.* **2014,** *136* , 14107-14113.
19. Kyriacou, G.; Anagnostopoulos, A., Electrochemical reduction of CO_2 at Cu + Au electrodes. *J. Electroanal. Chem.* **1992,** *328*, 233-243.
20. Ogura, K.; Yano, H.; Shirai, F., Catalytic reduction of CO_2 to ethylene by electrolysis at a three-phase interface. *J. Electrochem. Soc.* **2003,** *150*, D163-D168.
21. Y. Hori; A. Murata; R. Takahashi; Suzuki, S., Enhanced formation of ethylene and alcohols at ambient temperature and pressure in electrochemical reduction of carbon dioxide at a copper electrode. *J. Chem. Soc., Chem. Commun.* **1988**, *0*, 17-19.
22. Varela, A. S.; Kroschel, M.; Reier, T.; Strasser, P., Controlling the selectivity of CO_2 electroreduction on copper: The effect of the electrolyte concentration and the importance of the local pH. *Catal. Today* **2016,** *260*, 8-13.
23. Singh, M. R.; Kwon, Y.; Lum, Y.; Ager, J. W., III; Bell, A. T., Hydrolysis of electrolyte cations enhances the electrochemical reduction of CO_2 over Ag and Cu. *J. Am. Chem. Soc.* **2016,** *138*, 13006-13012.
24. Gupta, N.; Gattrell, M.; MacDougall, B., Calculation for the cathode surface concentrations in the electrochemical reduction of CO_2 in $KHCO_3$ solutions. *J. Appl. Electrochem.* **2006,** *36*, 161-172.
25. Weast, R., *CRC Handbook of Chemistry and Physics*. 59th ed.; CRC Press: Boca Raton, FL, 1979.
26. Schulz, K. G.; Riebesell, U.; Rost, B.; Thoms, S.; Zeebe, R. E., Determination of the rate constants for the carbon dioxide to bicarbonate inter-conversion in pH-buffered seawater systems. *Mar. Chem.* **2006,** *100*, 53-65.
27. Verma, S.; Lu, X.; Ma, S.; Masel, R. I.; Kenis, P. J., The effect of electrolyte composition on the electroreduction of CO_2 to CO on Ag based gas diffusion electrodes. *Phys. Chem. Chem. Phys.* **2016,** *18*, 7075-7084.
28. Zhong, H.; Fujii, K.; Nakano, Y.; Jin, F., Effect of CO_2 bubbling into aqueous solutions used for electrochemical reduction of CO_2 for energy conversion and storage. *J. Phys. Chem. C* **2015,** *119*, 55-61.

29. Janssen, L. J. J.; Hoogland, J. G.; The effect of electrolytically evolved gas bubbles on the thickness of the diffusion layer-II. *Electrochimia Acta* **1973**, *18*, 543-550.

$$CO_2 + H_2O + 8e^- \rightarrow CH_4 + 8OH^-$$

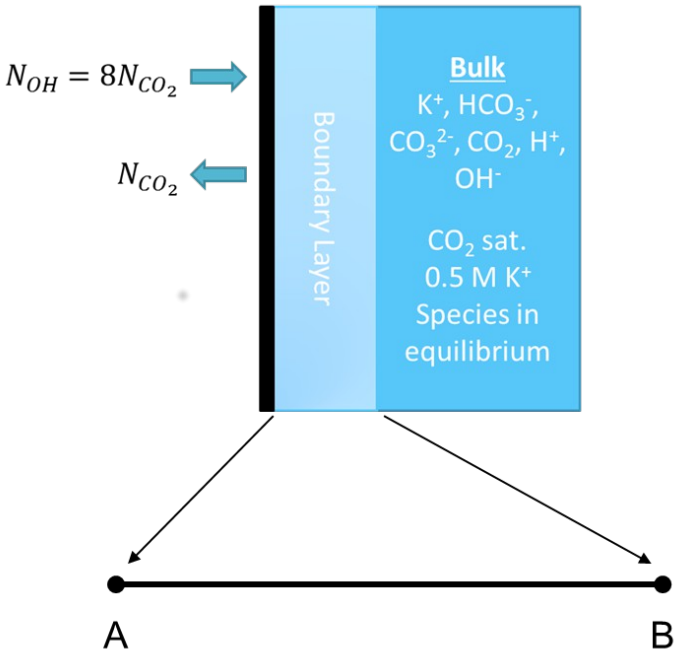

Figure 1. Schematic illustration of 1-D simulation model assuming 100% CH_4 faradaic efficiency

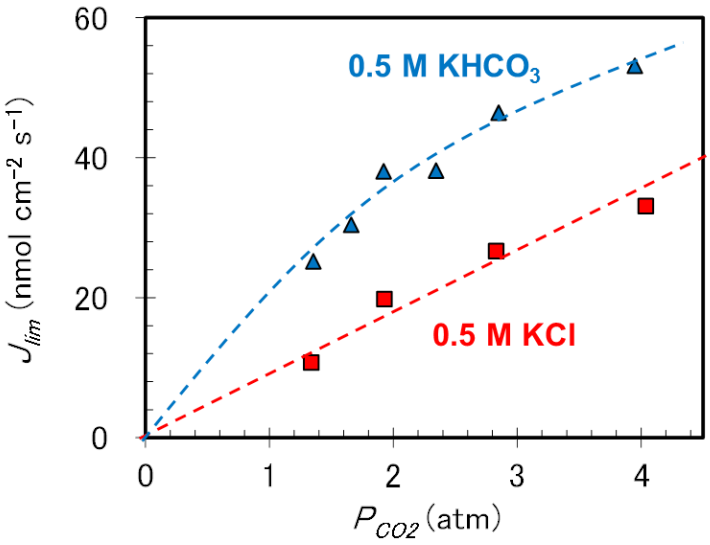

Figure 2. CO_2 pressure (P_{CO2}) dependence of limiting rate of mass transport of CO_2 (J_{lim}) in 0.5M $KHCO_3$ (blue triangles) and 0.5M KCl (red squares) solutions (dotted lines are guides for the eye only).

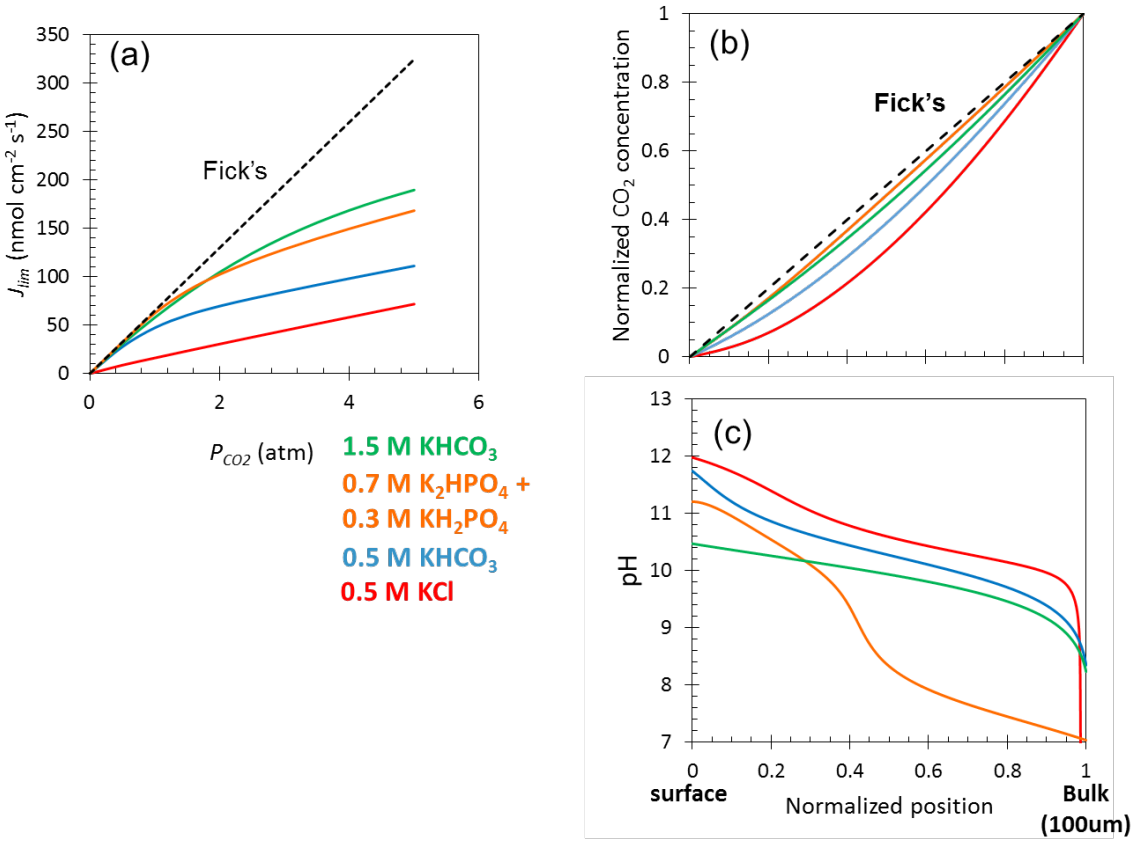

Figure 3. (a) Model results (assuming 100% conversion of CO_2 to CH_4) of CO_2 pressure dependence of J_{lim} in 4 different electrolytes; the dotted line indicates assuming Fick's law. (b) CO_2 concentration and (c) pH within the 100 μm boundary layer at P_{CO2} of 2 atm.

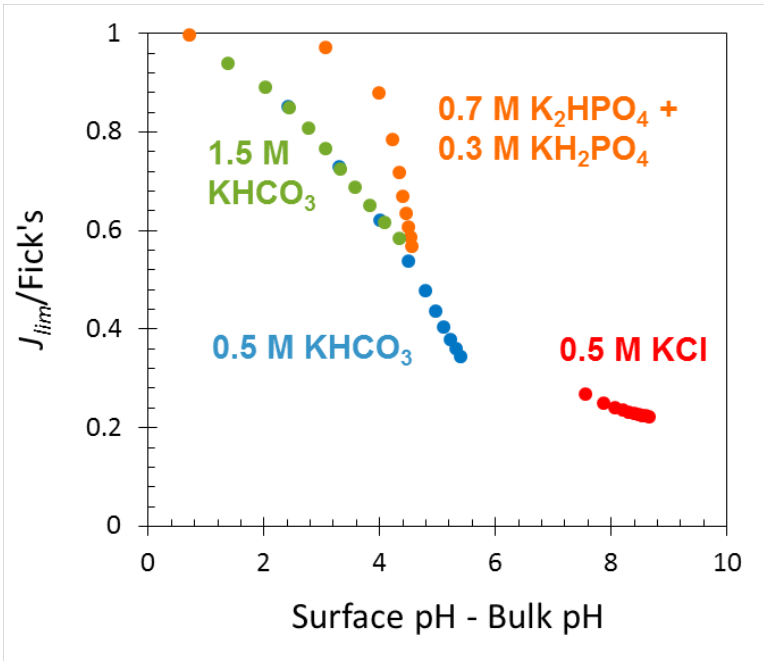

Figure 4. Relationship between normalized J_{lim} (to that expected from Fick's law) and pH change within the boundary layer for 4 different electrolytes.

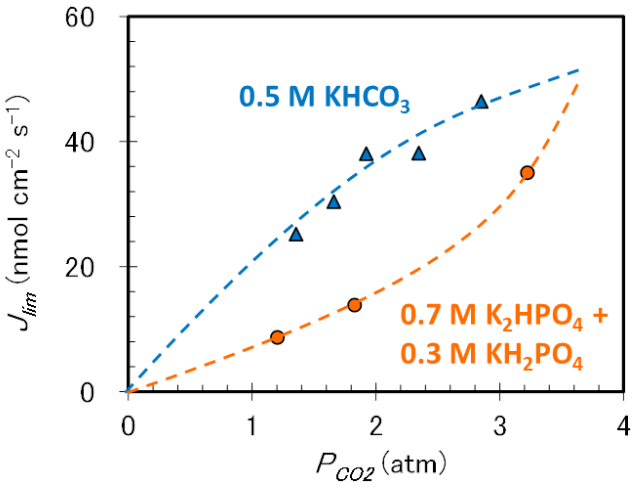

Figure 5. Experimental results of P_{CO2} dependence of J_{lim} in 1 M phosphate buffer (orange circles) compared to 0.5 M $KHCO_3$ (blue triangles).

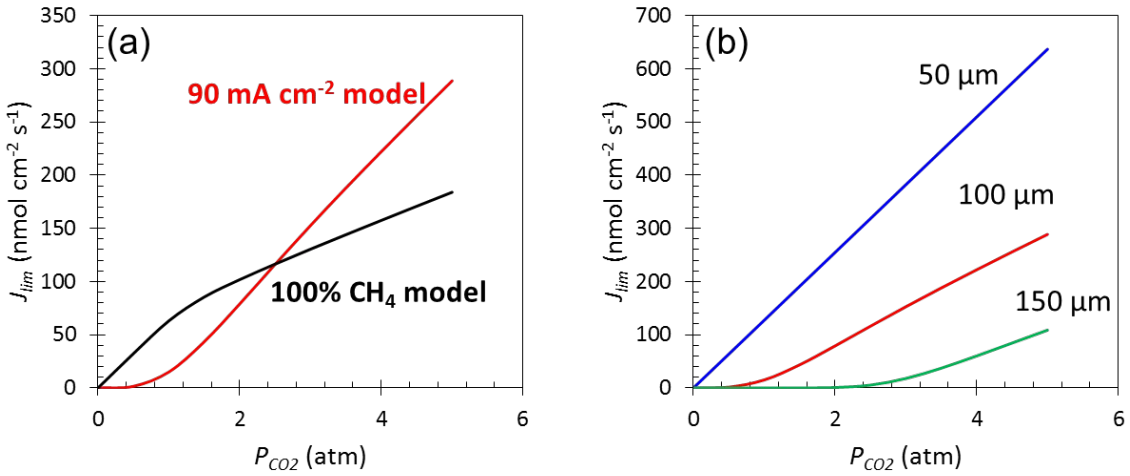

Figure 6 (a) Comparison of pressure dependence of J_{lim} between 100% CO_2 reduction and constant OH^- flux (corresponding to 90 mA cm^{-2}) models with the phosphate buffer solution and 100 µm boundary-layer thickness. (b) The effect of boundary-layer thickness on the pressure dependence of J_{lim} using the constant OH^- flux model with phosphate buffer solution.

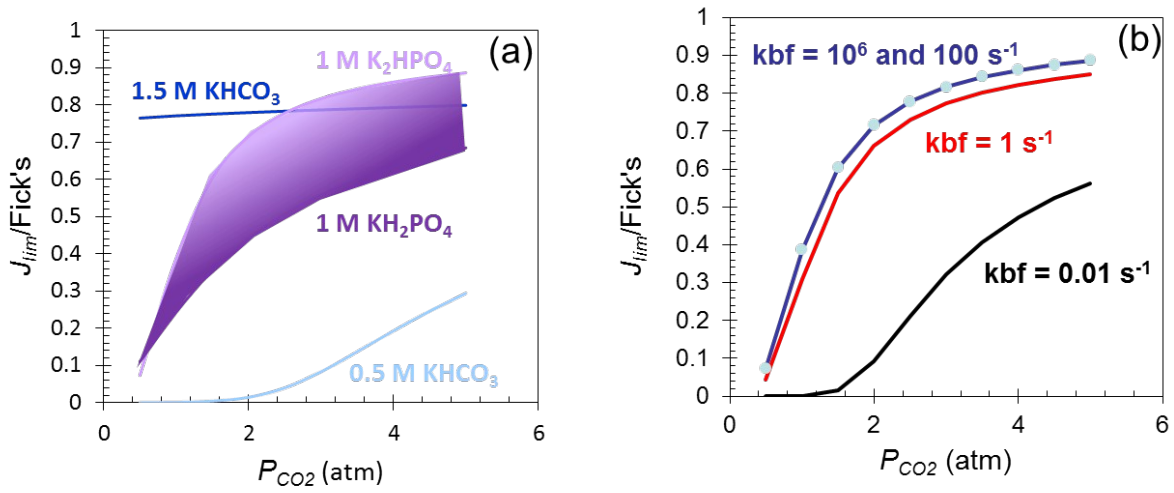

Figure 7. Comparison of pressure dependence of J_{lim} for (a) 0.5 and 1.5 M $KHCO_3$ and a range of 1 M phosphate from K_2HPO_4 to KH_2PO_4 (purple area) and (b) as a function of phosphate buffer kinetic rates (see equation 4) using 1 M K_2HPO_4. All simulations done assuming 90 mA/cm^2 total current density.

Table 1. Boundary conditions for the 1-D models.

	100% CH_4 model	**Constant current density model**
Electrode boundary	$c_{CO_2}=0$ $OH^{-¿}=-8N_{CO_2}$ $N_{¿}$ $N_i=0, i\neq CO_2, OH^{-¿}$	$c_{CO_2}=0$ $OH^{-¿}=-i_T/F$ $N_{¿}$ $N_i=0, i\neq CO_2, OH^{-¿}$
Bulk electrolyte boundary	$N_i=-k_i\left(c_i-c_i^b\right)$ $\phi_l=0$	

”TOC Graphic”

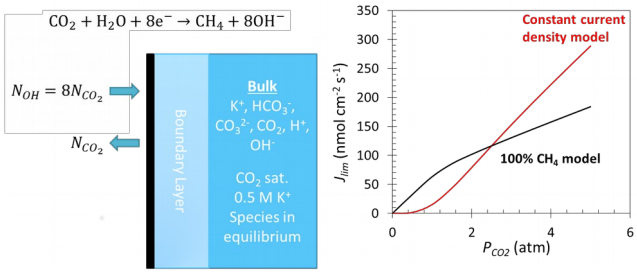
$CO_2 + H_2O + 8e^- \rightarrow CH_4 + 8OH^-$
$N_{OH} = 8N_{CO_2}$
N_{CO_2}
Boundary Layer
Bulk
K^+, HCO_3^-, CO_3^{2-}, CO_2, H^+, OH^-
CO_2 sat. 0.5 M K^+ Species in equilibrium
Constant current density model
100% CH_4 model
J_{lim} (nmol cm^{-2} s^{-1})
P_{CO2} (atm)
0
50
100
150
200
250
300
350
0
2
4
6